NANO LETTERS
Letter
Cite This: Nano Lett. 2019, 19, 538−544
pubs.acs.org/NanoLett

Antimony Nanorod Encapsulated in Cross-Linked Carbon for High-Performance Sodium Ion Battery Anodes

Chunyu Cui,[†,‡,§] Jiantie Xu,*[,‡] Yiqiong Zhang,[§] Zengxi Wei,[§] Minglei Mao,[†] Xin Lian,[‡] Shuangyin Wang,[§] Chongyin Yang,[†] Xiulin Fan,[†] Jianmin Ma,*[,§] and Chunsheng Wang*[,†]

[†]Department of Chemical and Biomolecular Engineering, University of Maryland, College Park, Maryland 20742, United States
[‡]School of Environment and Energy, South China University of Technology, Guangzhou 510640, China
[§]School of Physics and Electronics, Hunan University, Changsha 410082, China

Supporting Information

ABSTRACT: Antimony- (Sb) based materials have been considered as one of promising anodes for sodium ion batteries (SIBs) owing to their high theoretical capacities and appropriate sodium inserting potentials. So far, the reported energy density and cycling stability of the Sb-based anodes for SIBs are quite limited and need to be significantly improved. Here, we develop a novel Sb/C hybrid encapsulating the Sb nanorods into highly conductive N and S codoped carbon (Sb@(N, S−C)) frameworks. As an anode for SIBs, the Sb@(N, S−C) hybrid maintains high reversible capacities of 621.1 mAh g^{-1} at 100 mA g^{-1} after 150 cycles, and 390.8 mAh g^{-1} at 1 A g^{-1} after 1000 cycles. At higher current densities of 2, 5, and 10 A g^{-1}, the Sb@(N, S−C) hybrid also can display high reversible capacities of 534.4, 430.8, and 374.7 mAh g^{-1}, respectively. Such impressive sodium storage properties are mainly attributed to the unique cross-linked carbon networks providing highly conductive frameworks for fast transfer of ions and electrons, alleviating the volume expansion and preventing the agglomeration of Sb nanorods during the cycling.

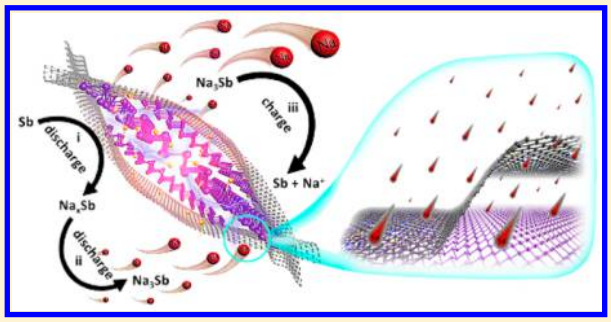

KEYWORDS: *Antimony, nanorods, co-doping, carbon networks, sodium ion batteries*

In recent years, sodium ion batteries (SIBs) have attracted great attention as one of most promising cost-effective energy storage devices.[1] This is mainly due to rich natural resources of sodium and similar ion insertion mechanism of SIBs to well-developed lithium ion batteries (LIBs).[2] Compared to the counterparts of LIBs, the anode performances of SIBs are still unsatisfied and need to be significantly improved, though a large number of anode candidates have been explored, including carbon-based materials (e.g., graphite,[3] graphene,[4] and carbon nanowires[5]), metal oxides and sulfides (e.g., TiO_2,[6] $NiCo_2O_4$,[7] V_5S_8,[8] and MoS_2[9]), elements (e.g., P,[10] Sb,[11] and Sn[12]), and other compounds (e.g., Ti_3C_2[13] and $NaTi_2(PO_4)_3$[14]). Among these reported anodes, metallic Sb has attracted considerable interest because of its high theoretical capacity (Na_3Sb, 660 mAh g^{-1}) and appropriate sodium inserting potential range of 0.5−0.8 V versus Na^+/Na.[15] Nevertheless, the large volume change (up to ∼300 vol % from Sb → Na_3Sb) during the Na^+ insertion/extraction process severely hinders their applications in SIBs.[16] To address this critical issue, many strategies have been developed, such as the morphology and structure control (e.g., Sb nanorod arrays,[16] nanoporous Sb[17] and monodisperse Sb nanocrystals[18]), the hybridization of Sb with highly conductive carbon (e.g., carbon nanotubes,[19] graphene,[20] and amorphous carbon[21]), the alloying of Sb-based intermetallics (e.g., Bi,[22] Sn,[23] and Ge[24]), and in combination of them.[25] Carbon-based materials as ideal candidates are often used as matrix-to-hybrid with various metal-based nanoparticles. This is mainly due to the extraordinary electronic conductivity, high specific surface area, and stable chemical properties of carbon.[26−28] Sb@C coaxial nanotubes have been reported, although excellent sodium storage properties were obtained, the synthetic procedure was cumbersome when combining the hydrothermal and annealing method.[29] In addition, inspired by the application of doped carbon-based materials as anodes for SIBs, the coated carbon layer should be further modified for a better performance.[30] For the construction of carbon-based materials, the doping heteroatoms (e.g., N,[31] S,[32] F,[33] and P[34]) into carbon frameworks have been widely proven to significantly improve sodium storage properties of the carbon-based materials. Among these heteroatoms, N atom with higher electronegativity (χ = 3.04) than C atom (χ = 2.55) have gained more attention. This is because the N-doping could significantly increase the conductivity of carbon and induce the charge redistribution at N−C sites, thus leading to the enhanced Na^+ storage performance.[31] Besides N, the

Received: November 5, 2018
Revised: December 7, 2018
Published: December 14, 2018

DOI: 10.1021/acs.nanolett.8b04468
Nano Lett. 2019, 19, 538−544

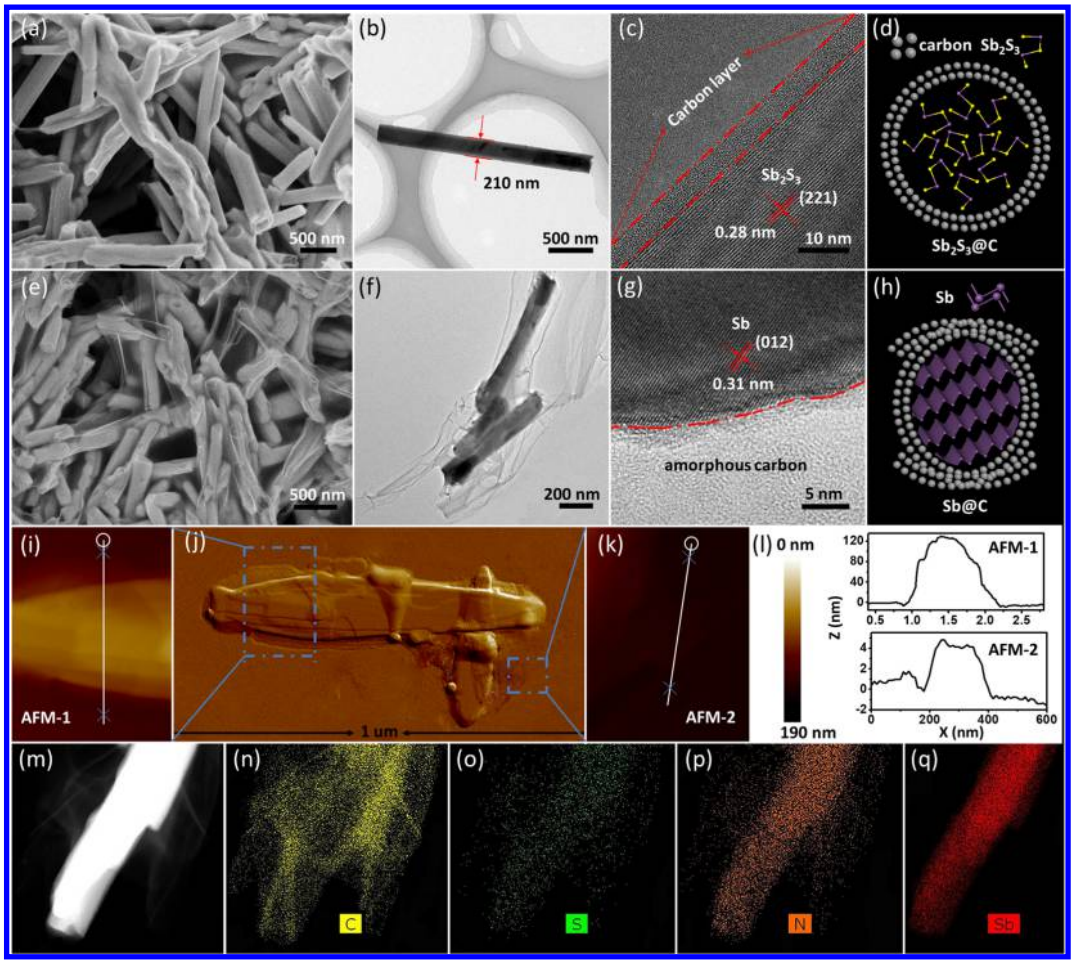

Figure 1. (a,e) SEM images, (b,f) TEM images, (c,g) HRTEM images, and (d,h) schematic representation of (a−d) Sb_2S_3@C (500 °C) and (e−h) Sb@(N,S−C)-2. (j) AFM image of Sb@(N, S−C)-2, (i,k) its selected areas, and (l) corresponding height profile along the white line overlaid in (i,k). (m−q) Elemental mapping images of (m) Sb@(N, S−C)-2: (n) C, (o) S, (p) N, and (q) Sb.

doping of S into C also enhances the sodium ion storage properties of carbon for SIBs. Compared to C (χ = 2.55 and d = 77 pm), S has a larger atomic radius of 102 pm and higher electronegativity.[35] As expected, the S-doping could provide the enlarged interlayer distance for carbon nanosheets, as well as the creation of structural defects and delocalization of electrons within the carbon framework, thus leading to rapid diffusion of Na^+ and extra active sites for Na^+ storage. In particular, recent advances in the heteroatoms codoped (e.g., N and P,[30] N and S,[36] N and F[37]) into carbon nanomaterials with enhanced electrochemical performance have inspired further explorations of doped carbon anodes.

Under these situations, herein we designed and synthesized Sb nanorods encapsulated in N, S codoped ultrathin carbon networks (Sb@(N, S−C)). Figure S1 shows the scheme of the fabrication process of the Sb@(N, S−C) hybrid. The Sb@(N, S−C) hybrid was fabricated by simply annealing the mixture solution of superfluous thioacetamide (TAA), antimony acetate (AA), and edetic acid (EDTA) in ethylene glycol (EG) at 800 °C for 2h in argon atmosphere. As shown in Figures S2 and S3, with EG as a nucleophilic solvent, the S^{2-} from TAA reacts with Sb^+ from AA to form Sb_2S_3 nuclei along the c-axis. The inherent layered-type structure of stibnite enables the formation of the rodlike Sb_2S_3@C core−shell structure[38,39] in which the Sb_2S_3 nanorod is uniformly coated by a carbon layer. In the annealing process, the Sb_2S_3 is further reduced to Sb by carbon and simultaneously transferred to interconnected Sb nanorods encapsulated by heteroatom co-doped carbon (N, S−C). The onestep-synthetic procedure was very convenient. As expected, such a "rodlike" structure not only effectively enhances the electronic conductivity of the electrode but also alleviates the volume expansion of Sb during the sodiation−desodiation process. Moreover, the N, S-co-doped carbon networks between Sb@(N, S−C) nanorods are favorable for the enhancement of the electrode conductivity, preservation of the structural integrity, and the suppression of the Sb agglomeration during the cycling process.

To investigate the impact of carbon content the Sb@(N, S−C) hybrids, different mass ratios of EDTA/(TAA + AA) (0.5:9, 1:9, and 1.5:9, g) were used and the resultant Sb@(N, S−C) materials are denoted as Sb@(N, S−C)-1, Sb@(N, S−C)-2, and Sb@(N, S−C)-3, respectively.

Figures 1 and S2 show scanning electron microscopy (SEM) and transmission electron microscopy (TEM) images of the Sb_2S_3@C precursors at 500 °C and Sb@(N,S−C)-2. As shown Figure 1a,b, the diameter of Sb_2S_3@C nanorod at 500 °C is ∼210 nm. High-resolution TEM (HRTEM) image (Figure 1c) reveals an estimated lattice spacing of ∼0.28 nm for the Sb_2S_3 nanorod, corresponding to the (221) plane of Sb_2S_3.[40] An amorphous carbon film with a thickness of ∼5 nm uniformly coated on the surface of Sb_2S_3 is also clearly observed in HRTEM. Compared to Sb_2S_3@C, the Sb nanorod in the

DOI: 10.1021/acs.nanolett.8b04468
Nano Lett. 2019, 19, 538−544

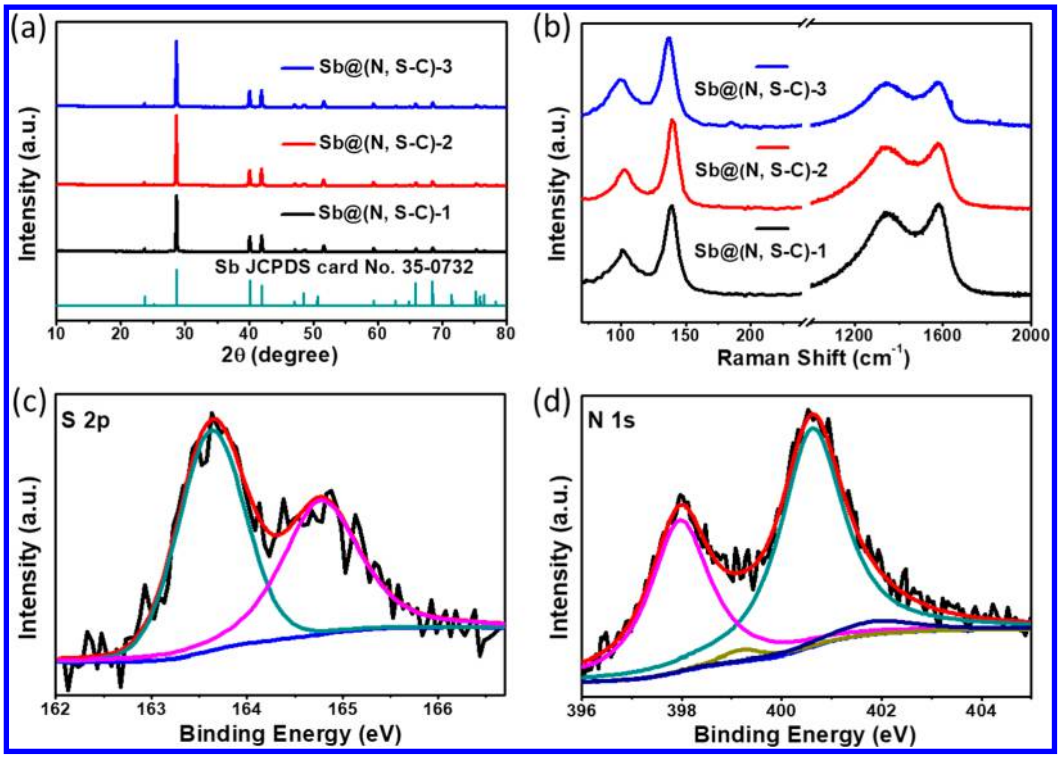

Figure 2. (a) XRD patterns and (b) Raman spectra of Sb@(N, S−C)-1, Sb@(N, S−C)-2, and Sb@(N, S−C)-3. High-resolution XPS spectra of Sb@(N, S−C)-2: (c) S 2p and (d) N 1s.

Sb@(N, S−C)-2 has the reduced rod size with a diameter of 120−160 nm (Figure 1f). Moreover, the "silk-like" carbon networks in the Sb@(N, S−C)-2 hybrid are nonuniformly distributed around the Sb nanorods, however, they can be regarded as a highly conductive bridge for each Sb@C nanorod. HRTEM image of Sb@(N, S−C)-2 (Figure 1g) further reveals the amorphous carbon and a clear lattice (∼0.31 nm) corresponding to the plane (012) of Sb. The existence of hollow carbon networks in Sb@(N, S−C)-2 is due to the Sb volatilization. The thickness of the Sb in Sb@(N, S−C)-2 was further determined using atomic force microscope (AFM) (Figure 1i−l). As can be seen, the thickness of Sb nanorod is ∼130 nm in Figure 1i,l (top), which is consistent with TEM results (Figure 1f). The thicknesses of carbon coating on the surface of Sb@(N, S−C)-2 is only 1−5 nm (bottom of Figure 1i,l). Furthermore, the elemental mappings of Sb@(N, S−C)-2 (Figure 1m−q) also confirm the uniform distribution of N, S, C, and Sb, in Sb@(N, S−C)-2 hybrid.

Figure 2a presents the X-ray diffraction (XRD) patterns of Sb@(N, S−C)-1, Sb@(N, S−C)-2, and Sb@(N, S−C)-3. As can be seen, the sharp XRD peaks of all the hybrids can be well indexed to hexagonal structured Sb (JCPDS card No. 35-0732).[16] Raman spectra (Figure 2b) also display typical signals of Sb at ∼101 and ∼138 cm^{-1}, and two characteristic peaks of the carbon centering at ∼1343 cm^{-1} (D-band) and ∼1581 cm^{-1} (G-band).[17] The surface electronic states of Sb@(N, S−C)-2 were characterized using X-ray photoelectron spectroscopy (XPS). As shown in Figure S4, all XPS spectra of the Sb@(N, S−C)-2 (Figure S4g−i) show the strong characteristic peaks of Sb $3d_{5/2}$ at ∼528.0 (Sb metal) and ∼530.2 eV (Sb oxidization), Sb $3d_{3/2}$ at ∼537.3 (Sb metal), and ∼539.5 eV (Sb oxidization). C 1s at ∼284.0 eV is also observed (Figure S4m−o).[11,17] The S $2p_{3/2}$ at ∼161.7 eV and S $2p_{1/2}$ at ∼162.9 eV in the S 2p XPS peaks of Sb@(N, S−C)-2 (Figure 2c) can be assigned to −C−S−C− covalent bond.[41] In addition, the existence of pyridinic N at ∼398.0, pyrrolic N at ∼400.7, and graphitic N at ∼401.9 eV[42] are also confirmed in Figure 2d.

Figure 3a shows initial five cycles cyclic voltammogram (CV) curves of Sb@(N, S−C)-2 at a scan rate of 0.1 mV s^{-1} between 0.01 and 2.50 V. During the first cathodic scan, a sharp peak at ∼0.27 V is clearly observed, which can be ascribed to the alloy of Sb with Na forming Na_xSb and the formation of a solid electrolyte interphase (SEI) layer.[16] In the subsequent cycles, two new reduction peaks appear at ∼0.66 and ∼0.52 V. This is due to the multistep conversion from Sb to Na_xSb ($x \leq 3$) and deep sodiation to $Na_{3+x}Sb$. The increased alloy reaction potential of Sb with Na after the first charge/discharge cycle is due to reduced stress/strain after formation of cracks in the first sodiation−desodiation cycle.[16] During the anodic scan, the broad peak at ∼0.9 V is attributed to the extraction of Na^+ from Na_xSb. These similar electrochemical behavior are also observed from the CV curves of Sb@(N, S−C)-1 and Sb@(N, S−C)-3 electrodes (Figure S7). Figure 3b displays the galvanostatic discharge/charge curves of the Sb@(N, S−C)-2 at a current density of 100 mA g^{-1} in the voltage range of 0.01−2.50 V. As can be seen, the capacity loss in the first discharge/charge cycle is mainly due to the irreversible formation of the SEI film. The observed distinct two obvious discharge−charge plateaus correspond to the phase changes in successive Li−Sb alloying processes, which agrees well with the two peaks in the corresponding CV curve (Figure 3a).

In order to further investigate the phase changes and the reaction mechanism, the Sb@(N, S−C)-2 electrodes at different states of charge/discharge in the first three cycles were analyzed using in situ XRD. As shown in Figure 3c, at stage I (i.e., discharged to 0.75 V), the intensities of three main Sb peaks at ∼28.7°, ∼39.9°, and ∼41.9° become weaker and

DOI: 10.1021/acs.nanolett.8b04468
Nano Lett. 2019, 19, 538−544

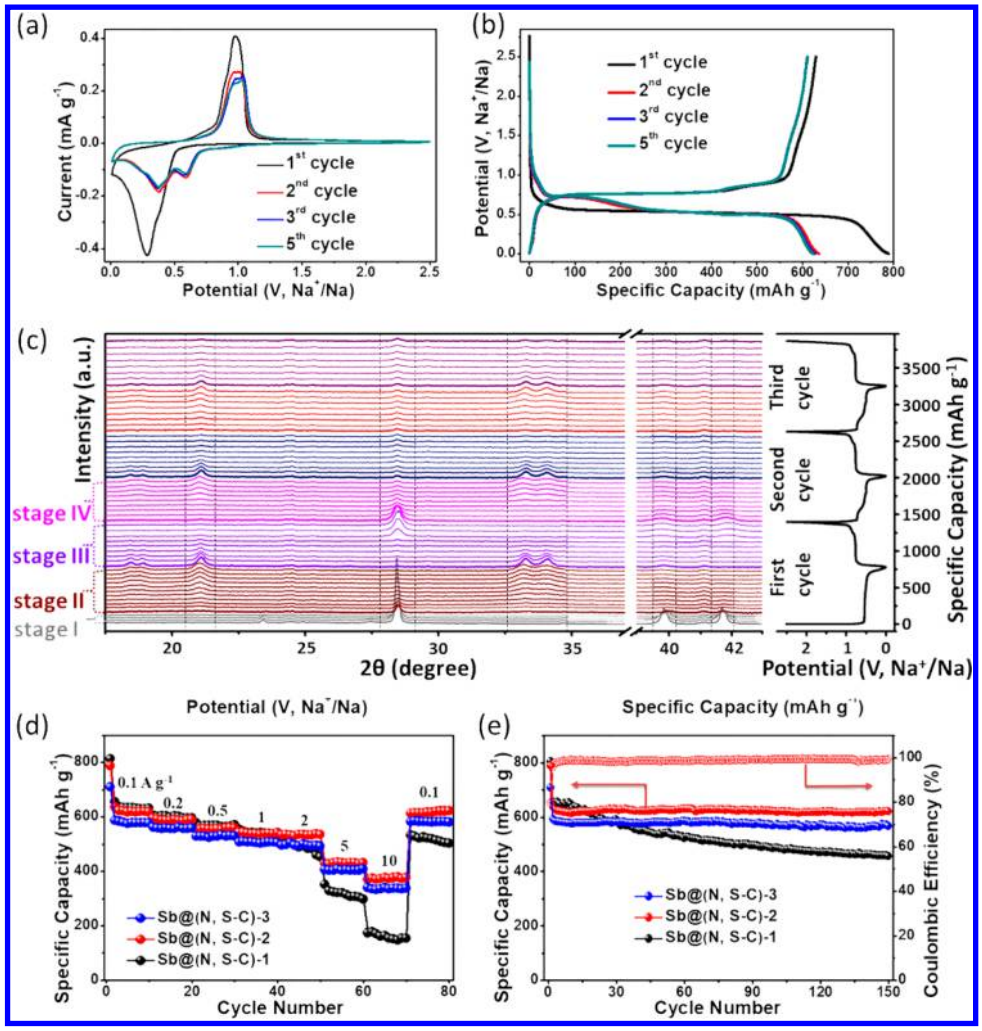

Figure 3. (a) CV curves at 0.1 mV s^{-1} and (b) discharge−charge profiles of Sb@(N, S−C)-2 for initial five cycles. (c) In situ XRD measurements of Sb@(N, S−C)-2 for initial three cycles. (d) Rate capability at various current densities from 0.1 to 10 A g^{-1}, and (e) cycling performance at 0.1 A g^{-1} of Sb@(N, S−C)-1, Sb@(N, S−C)-2, and Sb@(N, S−C)-3.

there are no new peaks appearing, indicating the formation of Na_xSb with increasing amounts of amorphous patterns.[15,43,44] From 0.75 to 0 V (stage II), new broad peaks at ∼18.5°, ∼18.9°, ∼21.1°, ∼33.3°, and ∼34.1° due to the formation of Na_3Sb are gradually increased, however, the peak at ∼28.7° becomes weaker until it disappears at 0.0 V.[15,45] The decrease in intensity of these XRD peaks well supports that the sodiation of Sb follows the mechanism of Sb → Na_xSb→ Na_3Sb. In the subsequent charge process (stage III), the charateristic peaks of Na_3Sb at ∼18.5°, ∼18.9°, ∼21.1°, ∼33.3°, and ∼34.1° gradually vanish while the peaks assigned to Sb at ∼28.7°, ∼ 39.9°, and ∼41.9° gradually recover, corresponding to the reversible desodiation reaction of Na_3Sb → Sb. However, the XRD peak intensity of the Sb at the end of stage III is still significantly lower than that in the pristine electrode. The continuous decrease in the intensity of XRD peaks in the subsequent cycles demonstrate that the amorphous Sb is accumulated during the sodiation−desodiation cycles.

The rate capabilities of Sb@(N, S−C) were evaluated at various current densities from 0.1 to 10 A g^{-1} in the voltage range of 0.01−2.5 V (Figure 3d). At 0.1 A g^{-1}, the Sb@(N, S−C)-1, Sb@(N, S−C)-2, and Sb@(N, S−C)-3 deliver high discharge capacities of 812.7, 787.4, and 709.2 mA h g^{-1}, respectively. When the current density is raised from 0.1 to 10 A g^{-1}, the Sb@(N, S−C)-2 exhibts the best rate capability with average reversible capacities of 638.7, 588.9, 556.6, 540.1, 534.4, 430.8, and 374.7 mAh g^{-1} at 0.1, 0.2, 0.5, 1, 2, 5, and 10 A g^{-1}, respectively. Sb@(N, S−C)-1 shows the worst rate behavior most likely due to the lowest carbon content in Sb@(N, S−C)-1. This could not preserve the electrode integrity during the repeat volume changes in the sodiation−desodiation process. However, too thick of a carbon coating in the Sb@(N, S−C)-3 is not favorable for the sodium ions' transportation and thus is fatal to the rate capacity. Moreover, large amounts of carbon also reduce the capacity contribution from the Sb. When the current density is reduced back to 0.1 A g^{-1}, capacities of Sb@(N, S−C)-2 and Sb@(N, S−C)-3 hybrids return to their initial values, demonstrating robustness to tolerate the current changes. The cycling stability of the Sb@(N, S−C) hybrids at 0.1 A g^{-1} was compared in Figure 3e. As can be seen, Sb@(N, S−C)-2 has the best cycling stability in 150 cycles. The long-term cycling performance of Sb@(N, S−C)-2 at a high current of 1 A g^{-1} was also evaluated. After 1000 cycles, the hybrid still retains a reversible capacity of 390.8 mA h g^{-1} (Figure S8). The structural robustness of cycled Sb@(N, S−C)-2 electrode was further evidenced by its

DOI: 10.1021/acs.nanolett.8b04468
Nano Lett. 2019, 19, 538−544

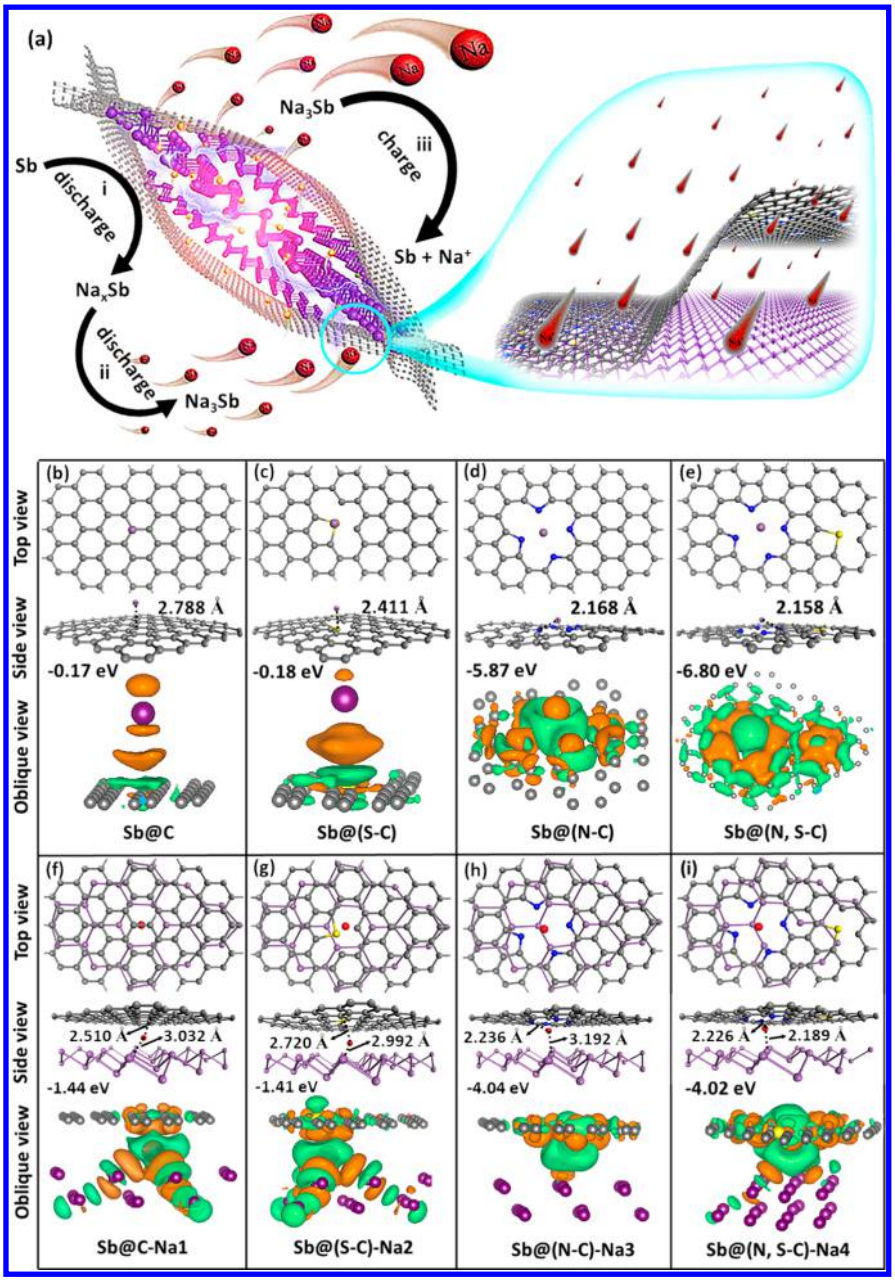

Figure 4. (a) Scheme of the reaction mechanism during the charge/discharge process for Sb@(N, S−C). (b−e) Four feasible models for optimal adsorption sites of Sb atom on single C layer. (f−i) Four feasible models for optimal adsorption sites of Na^+ between the C layer and the Sb layer.

well-preserved electrode morphology after 150 cycles (Figure S9).

Figure 4b−e shows the adsorption energies of a Sb atom in these four models. The lower adsorption energy indicates strong and preferential adsorption ability. As expected, the Sb−C with low adsorption energy could effectively decrease the Sb splitting up from the C layer during the Na^+ insertion/extraction. As can be seen, the adsorption energy for Sb@(N, S−C) (−6.80 eV) is much smaller than those for Sb@(N−C) (−5.87 eV), Sb@(S−C) (−0.18 eV), and Sb@C (−0.17 eV), indicating the superiority and strong synergistic effect of the N, S codoping.[31,35] Moreover, to verify the sodium storage properties of Sb@(N, S−C) influenced by N, S codoping into the 2D C layer, nine feasible models were also developed, as shown in Figures 4f−i and S10. When the Na^+ is adsored between the C layer and the Sb layer (Figure 4f−i), the Sb@(N−C)-Na3 (−4.04 eV) and Sb@(N, S−C)-Na4 (−4.02 eV) show the lower adsorption energies than Sb@C−Na1 (−1.44 eV) and Sb@(S−C)-Na2 (−1.41 eV). When the Na^+ is adsorbed upon the pure Sb layer (Figure S10a) and the C layer of Sb@C (Figure S10b−f), the adsorption energies for the Sb@Na5, Sb@C−Na6, Sb@(S−C)-Na7, Sb@(N−C)-Na8 and Sb@(N, S−C)-Na9 are −1.26, −0.83, −0.86, −4.99, and −5.00 eV, respectively. From these results (Figures 4f−i and S10), the enhanced Na^+ adsorption on the Sb@(N, S−C) is mainly induced by the N doping rather than S doping. Despite this, the Na^+ adsorption energy upon the C layer of the Sb@(N, S−C)-Na9 (−5.00 eV) is not significantly decreased by the introduction of S doping (−0.86 eV), compared to Sb@(N -C)-Na8 (−4.99 eV). When Na^+ adsorbed between C layer and Sb layer, the adsorption energy of Sb@(N, S−C)-Na4 (−4.02 eV) is even higher than Sb@(N−C)-Na3 (−4.04

DOI: 10.1021/acs.nanolett.8b04468
Nano Lett. 2019, 19, 538−544

eV). This is because the S doping within Sb@(N, S−C) probably changes the charge and spin densities of carbon,[46] which is believed to contribute to the enhanced sodium storage properties. Therefore, the codoping of N and S in the carbon (N, S−C) provides more significant contribution to adsorb Sb without sacrificing the sodium storage properties of Sb@(N, S−C), leading to the enhanced electrochemical performance.

In summary, the Sb@(N, S−C) hybrids in which Sb nanorods are uniformly coated with highly conductive and cross-linked N, S codoped carbon networks were synthesized using a simple but effective method. The Sb@(N, S−C)-2 hybrid as the anode for SIBs maintains a high reversible capacity of 621.1 mAh g^{-1} at 100 mA g^{-1} after 150 cycles and 390.8 A g^{-1} at 1 A g^{-1} after 1000 cycles. In addition, the Sb@(N, S−C)-2 still displays a high capacity of 534.4, 430.8, and 374.7 mAh g^{-1} when the current densities are increased to 2, 5, and 10 A g^{-1}, respectively. The outstanding electrochemical performance was attributed to the unique cross-linked carbon frameworks, which provides conductive frameworks for the adsorption of Sb nanorods, rapid diffusion of ions and electrons, alleviation of the volume changes, and prevention of the Sb nanorods agglomeration during the cycles. Moreover, the N, S codoping to carbon not only enables the hybrid with improved conductivity and adsorption abilities for Sb and Na^+ but also creates extra active sites for Na^+ storage. As expected, the as-synthesized Sb@(N, S−C) hybrid makes it promising as a high-performance anode for SIBs in the future.

■ ASSOCIATED CONTENT

Supporting Information

The Supporting Information is available free of charge on the ACS Publications website at DOI: 10.1021/acs.nanolett.8b04468.

Details of experimental method, characterizations, electrochemistry, and additional figures (PDF)

■ AUTHOR INFORMATION

Corresponding Authors

*E-mail: cswang@umd.edu.
*E-mail: jiantiexu@scut.edu.cn.
*E-mail: nanoelechem@hnu.edu.cn.

ORCID

Jiantie Xu: 0000-0002-5259-2760
Shuangyin Wang: 0000-0001-7185-9857
Chongyin Yang: 0000-0002-7127-3087
Chunsheng Wang: 0000-0002-8626-6381

Notes

The authors declare no competing financial interest.

■ ACKNOWLEDGMENTS

This work is supported by the "Young Talent Fellowship" program through South China University of Technology, the Fundamental Research Funds for the Central Universities (2018JQ06), the National Natural Science Foundation of China (Grant 51302079), and the National Natural Science Foundation of Hunan Province (Grant 2017JJ1008).

■ REFERENCES

(1) Hannan, M. A.; Hoque, M. M.; Mohamed, A.; Ayob, A. *Renewable Sustainable Energy Rev.* **2017**, *69*, 771−789.
(2) Yabuuchi, N.; Kubota, K.; Dahbi, M.; Komaba, S. *Chem. Rev.* **2014**, *114* (23), 11636−11682.
(3) Wen, Y.; He, K.; Zhu, Y.; Han, F.; Xu, Y.; Matsuda, I.; Ishii, Y.; Cumings, J.; Wang, C. *Nat. Commun.* **2014**, *5*, 4033.
(4) Yan, Y.; Yin, Y. X.; Guo, Y. G.; Wan, L. J. *Adv. Energy Mater.* **2014**, *4* (8), 1301584.
(5) Cao, Y.; Xiao, L.; Sushko, M. L.; Wang, W.; Schwenzer, B.; Xiao, J.; Nie, Z.; Saraf, L. V.; Yang, Z.; Liu, J. *Nano Lett.* **2012**, *12* (7), 3783−3787.
(6) Xiong, H.; Slater, M. D.; Balasubramanian, M.; Johnson, C. S.; Rajh, T. *J. Phys. Chem. Lett.* **2011**, *2* (20), 2560−2565.
(7) Alcántara, R.; Jaraba, M.; Lavela, P.; Tirado, J. L. *Chem. Mater.* **2002**, *14* (7), 2847−2848.
(8) Yang, C.; Ou, X.; Xiong, X.; Zheng, F.; Hu, R.; Chen, Y.; Liu, M.; Huang, K. *Energy Environ. Sci.* **2017**, *10* (1), 107−113.
(9) Hu, Z.; Wang, L.; Zhang, K.; Wang, J.; Cheng, F.; Tao, Z.; Chen, J. *Angew. Chem.* **2014**, *126* (47), 13008−13012.
(10) Qian, J.; Wu, X.; Cao, Y.; Ai, X.; Yang, H. *Angew. Chem.* **2013**, *125* (17), 4731−4734.
(11) Zhu, Y.; Han, X.; Xu, Y.; Liu, Y.; Zheng, S.; Xu, K.; Hu, L.; Wang, C. *ACS Nano* **2013**, *7* (7), 6378−6386.
(12) Wang, J. W.; Liu, X. H.; Mao, S. X.; Huang, J. Y. *Nano Lett.* **2012**, *12* (11), 5897−5902.
(13) Dong, Y.; Wu, Z. S.; Zheng, S.; Wang, X.; Qin, J.; Wang, S.; Shi, X.; Bao, X. *ACS Nano* **2017**, *11* (5), 4792−4800.
(14) Fang, Y.; Xiao, L.; Qian, J.; Cao, Y.; Ai, X.; Huang, Y.; Yang, H. *Adv. Energy Mater.* **2016**, *6* (19), 1502197.
(15) Darwiche, A.; Marino, C.; Sougrati, M. T.; Fraisse, B.; Stievano, L.; Monconduit, L. *J. Am. Chem. Soc.* **2012**, *134* (51), 20805−20811.
(16) Liang, L.; Xu, Y.; Wang, C.; Wen, L.; Fang, Y.; Mi, Y.; Zhou, M.; Zhao, H.; Lei, Y. *Energy Environ. Sci.* **2015**, *8* (10), 2954−2962.
(17) Liu, S.; Feng, J.; Bian, X.; Liu, J.; Xu, H. *Energy Environ. Sci.* **2016**, *9* (4), 1229−1236.
(18) He, M.; Kravchyk, K.; Walter, M.; Kovalenko, M. V. *Nano Lett.* **2014**, *14* (3), 1255−1262.
(19) Zhou, X.; Dai, Z.; Bao, J.; Guo, Y. G. *J. Mater. Chem. A* **2013**, *1* (44), 13727−13731.
(20) Hu, L.; Zhu, X.; Du, Y.; Li, Y.; Zhou, X.; Bao, J. *Chem. Mater.* **2015**, *27* (23), 8138−8145.
(21) Yang, C.; Li, W.; Yang, Z.; Gu, L.; Yu, Y. *Nano Energy* **2015**, *18*, 12−19.
(22) Zhao, Y.; Manthiram, A. *Chem. Mater.* **2015**, *27* (8), 3096−3101.
(23) Xiao, L.; Cao, Y.; Xiao, J.; Wang, W.; Kovarik, L.; Nie, Z.; Liu, J. *Chem. Commun.* **2012**, *48* (27), 3321−3323.
(24) Farbod, B.; Cui, K.; Kalisvaart, W. P.; Kupsta, M.; Zahiri, B.; Kohandehghan, A.; Lotfabad, E. M.; Li, Z.; Luber, E. J.; Mitlin, D. *ACS Nano* **2014**, *8* (5), 4415−4429.
(25) Liu, J.; Yang, Z.; Wang, J.; Gu, L.; Maier, J.; Yu, Y. *Nano Energy* **2015**, *16*, 389−398.
(26) Wenzel, S.; Hara, T.; Janek, J.; Adelhelm, P. *Energy Environ. Sci.* **2011**, *4* (9), 3342−3345.
(27) Tang, K.; Fu, L.; White, R. J.; Yu, L.; Titirici, M. M.; Antonietti, M.; Maier, J. *Adv. Energy Mater.* **2012**, *2* (7), 873−877.
(28) Balogun, M. S.; Luo, Y.; Qiu, W.; Liu, P.; Tong, Y. *Carbon* **2016**, *98*, 162−178.
(29) Liu, Z.; Yu, X. Y.; Lou, X. W.; Paik, U. *Energy Environ. Sci.* **2016**, *9* (7), 2314−2318.
(30) Zhang, C.; Wang, X.; Liang, Q.; Liu, X.; Weng, Q.; Liu, J.; Yang, Y.; Dai, Z.; Ding, K.; Bando, Y.; Tang, J.; Golberg, D. *Nano Lett.* **2016**, *16* (3), 2054−2060.
(31) Xu, J.; Wang, M.; Wickramaratne, N. P.; Jaroniec, M.; Dou, S.; Dai, L. *Adv. Mater.* **2015**, *27* (12), 2042−2048.
(32) Li, W.; Zhou, M.; Li, H.; Wang, K.; Cheng, S.; Jiang, K. *Energy Environ. Sci.* **2015**, *8* (10), 2916−2921.
(33) Wang, P.; Qiao, B.; Du, Y.; Li, Y.; Zhou, X.; Dai, Z.; Bao, J. *J. Phys. Chem. C* **2015**, *119* (37), 21336−21344.
(34) Song, J.; Yu, Z.; Gordin, M. L.; Li, X.; Peng, H.; Wang, D. *ACS Nano* **2015**, *9* (12), 11933−11941.

DOI: 10.1021/acs.nanolett.8b04468
Nano Lett. 2019, 19, 538−544

(35) Qie, L.; Chen, W.; Xiong, X.; Hu, C.; Zou, F.; Hu, P.; Huang, Y. *Adv. Sci.* **2015**, *2* (12), 1500195.
(36) Qiao, Y.; Ma, M.; Liu, Y.; Li, S.; Lu, Z.; Yue, H.; Dong, H.; Cao, Z.; Yin, Y.; Yang, S. *J. Mater. Chem. A* **2016**, *4* (40), 15565−15574.
(37) Peera, S. G.; Sahu, A. K.; Arunchander, A.; Bhat, S. D.; Karthikeyan, J.; Murugan, P. *Carbon* **2015**, *93*, 130−142.
(38) An, C.; Tang, K.; Yang, Q.; Qian, Y. *Inorg. Chem.* **2003**, *42* (24), 8081−8086.
(39) Chen, X.; Zhang, X.; Shi, C.; Li, X.; Qian, Y. *Solid State Commun.* **2005**, *134* (9), 613−615.
(40) Yu, D. Y. W.; Prikhodchenko, P. V.; Mason, C. W.; Batabyal, S. K.; Gun, J.; Sladkevich, S.; Medvedev, A. G.; Lev, O. *Nat. Commun.* **2013**, *4*, 2922.
(41) Yang, J.; Zhou, X.; Wu, D.; Zhao, X.; Zhou, Z. *Adv. Mater.* **2017**, *29* (6), 1604108.
(42) Xu, D.; Chen, C.; Xie, J.; Zhang, B.; Miao, L.; Cai, J.; Huang, Y.; Zhang, L. *Adv. Energy Mater.* **2016**, *6* (6), 1501929.
(43) Qian, J.; Chen, Y.; Wu, L.; Cao, Y.; Ai, X.; Yang, H. *Chem. Commun.* **2012**, *48* (56), 7070−7072.
(44) Ou, X.; Yang, C.; Xiong, X.; Zheng, F.; Pan, Q.; Jin, C.; Liu, M.; Huang, K. *Adv. Funct. Mater.* **2017**, *27* (13), 1606242.
(45) Songster, J.; Pelton, A. *J. Phase Equilib.* **1993**, *14* (2), 250−255.
(46) Jeon, I. Y.; Zhang, S.; Zhang, L.; Choi, H. J.; Seo, J. M.; Xia, Z.; Dai, L.; Baek, J. B. *Adv. Mater.* **2013**, *25* (42), 6138−6145.

DOI: 10.1021/acs.nanolett.8b04468
Nano Lett. 2019, 19, 538−544